Available online at www.sciencedirect.com
SCIENCE DIRECT®
Journal of Sound and Vibration 289 (2006) 1091–1111
JOURNAL OF SOUND AND VIBRATION
www.elsevier.com/locate/jsvi

# Modelling of sound propagation in a non-uniform lined duct using a Multi-Modal Propagation Method

W.P. Bi, V. Pagneux*, D. Lafarge, Y. Aurégan

*Laboratoire d'Acoustique de l'Université du Maine, UMR CNRS 6613, Av. O Messiaen, F-72085 Le Mans Cedex 9, France*

Received 14 November 2003; received in revised form 11 March 2005; accepted 11 March 2005
Available online 22 June 2005

**Abstract**

Liner non-uniformities, such as distributed impedances, may have a direct influence on the performance of turbofan engine liners. A relevant problem to study these effects is that of sound propagation in a hard-walled duct of circular cross-section, fitted with a region of non-uniform liner. Given the complex modal input amplitudes at one end of the hard-walled duct, the problem is to compute the complex modal output amplitudes at the other end. In the present paper, a Multi-Modal Propagation Method (MMPM) is proposed to solve this problem in the absence of mean flow. For simplicity, the liner impedance is set piecewise constant along the duct, while being arbitrarily variable along the circumference of each segment. The principle of the method is to expand the sound pressure and axial velocity into double infinite series using the rigid duct modal basis, and then to follow the projection coefficients evolution along the duct axis. Scattering matrices are obtained for individual segments and then combined to construct a global scattering matrix. It is numerically shown that the convergence rate of the infinite series is at least $O(M^{-2})$ and $O(N^{-1.5})$, where $M$ and $N$ refer to the maximum circumferential and radial mode orders, respectively. Validation of the method is done in 2D by comparison with FEM. The present MMPM is shown to deal with realistic turbofan engine configurations with spliced liners, up to relatively high reduced wavenumbers $K \sim 50$.


*Corresponding author. Fax: +33 2 43 83 35020.
*E-mail address:* vincent.pagneux@univ-lemans.fr (V. Pagneux).

0022-460X/$ - see front matter © 2005 Elsevier Ltd. All rights reserved.
doi:10.1016/j.jsv.2005.03.021

## 1. Introduction

In turbofan engine intakes, liners with longitudinal hard-walled splices are often used due to technological constraints. In-flight measurements [1] have indicated that sound radiation can be substantially modulated by the presence of splices. A relevant problem to study these effects is that of sound propagation in a hard-walled duct of circular cross-section, fitted with a region of non-uniform liner. The liner properties are assumed to be given by a distribution of locally reacting impedances. Without significant loss of generality, the distribution may be assumed axially segmented, i.e. the impedance is set piecewise constant along the duct, while being arbitrarily variable along the circumference of each segment (see Fig. 1). Given the complex modal input amplitudes at one end of the hard-walled duct, the problem is to compute the complex modal output amplitudes at the other end. In this paper, a simple Multi-Modal Propagation Method (MMPM) is proposed to solve this problem in the absence of flow.

In the presence of circumferential variations of the impedance (e.g. hard-walled splices), the problem to solve is fully 3D. Several approaches to it have been considered in the literature. Because the sound pressure and particle velocity field cannot be separated in the $r-\theta$ plane, the dispersion relation in one segment cannot be written explicitly, and it is not possible to use classical root finding routines to determine the eigenmodes. Watson [2] used a hard-walled duct mode expansion series to numerically evaluate the eigenmodes and axial wavenumbers. The Galerkin method was employed to force the series to satisfy the true boundary condition in the lined segment. The complex modal output amplitudes for a specified source distribution were then obtained by applying a mode-matching technique at the discontinuity between rigid and lined segments. Fuller [3,4] investigated the sound propagation and radiation in finite length of circumferentially non-uniform lined ducts. Representing the circumferential admittance function as a Fourier series and expanding the eigenmodes over the separable components adapted to the cylindrical coordinates, he obtained the eigen-equation set to be solved. The axial wavenumbers in the lined segment were then calculated by solving this set of equations using the method of Muller. Regan and Eaton [5] used a three-dimensional Finite Element Method (FEM) to address the problem of a longitudinally spliced liner. Scattering due to splices was clearly demonstrated in the transmitted modal spectra with the appearance of circumferential modes with orders different from the order of the excitation mode.

The MMPM we present here is a simple adaptation of the multimodal formulation or projection method proposed by Pagneux et al. [6] to model sound propagation in varying cross-section waveguides with rigid boundary conditions (see also Refs. [7–10] for other applications of the method to wave propagation in bends and the determination of Lamb waves in inhomogeneous elastic waveguides). In the absence of flow, the principle of the method is to project the acoustic first-order equations of motion over the modal basis of hard-walled duct and then to follow the evolution of the projection coefficients along the duct axis. Indeed, as a result of the linearized motion equations and local impedance boundary conditions, the vector composed of the pressure projections $\mathbf{P}$ obeys a second-order differential equation, $\mathbf{P}'' + \mathsf{A}\mathbf{P} = 0$, with piecewise constant, diagonal (hard-walled duct segment) or non-diagonal (lined duct segment) matrix $\mathsf{A}$. After truncation at a sufficient, fixed number of modes, the sound field may be conveniently expressed in each individual segment in terms of the eigenvalues and eigenvectors of matrix $\mathsf{A}$. Individual scattering matrices are used to express the reflection and transmission

coefficients of each segment, and then combined to obtain the global scattering matrix of the multi-segment system.

Validation of the present MMPM including the effects of lined impedance in the boundary conditions needs to be carefully done because the rigid duct modal basis does not satisfy the true boundary conditions after truncating the mode expansion. Moreover, the non-uniformities of lined impedance in axial and circumferential directions make the convergence behaviour to be more involved. For 2D (axisymmetric) configuration, the lining being independent of $\theta$, it is obvious that there are individual solutions $p = f(r,z)\mathrm{e}^{-\mathrm{j}m\theta}$. The true boundary conditions will be approached only at the expense of a summation over the radial index $n$. On the contrary, when the lining is circumferential non-uniform, the separation of variables $r, z$ and $\theta$ is no longer possible. The true boundary conditions will be approached at the expense of a mixed double summation over both indices $m$ and $n$. Zero mean flow is assumed for simplicity here; however, the method could be generalized to account for the presence of flow [11]. Questions related to the nonlinear dependence of lining properties on sound pressure level will not be addressed here (see e.g. Ref. [12] for a general review).

As compared to FEM codes, which involve spatial discretization in both the transverse and longitudinal directions, the present MMPM involves only discretization in the transverse directions (via the total number of modes selected in the calculation). This is a significant economy which enables applying the method at quite high reduced wavenumbers. Indeed, by using the MMPM we can calculate the noise propagation in the range of dimensionless wavenumber $K = kR \lesssim 50$ (where $k$ is the wavenumber and $R$ the duct radius) in which $K = 20$–$50$ is very important but is very difficult with FEM. As compared to modal approaches, which involve decomposing the field over the liner modes, the present MMPM involves only decomposing the field over a fixed basis. The use of one fixed, a priori known basis, eliminates the necessity of numerically doing mode matching at the interfaces between different segments. The eigenmodes need not be calculated beforehand to solve the propagation problem, but they can be determined if necessary, as hard-walled duct mode expansion series.

This paper is organized as follows. The mathematical details corresponding to the construction of the matrix $\mathsf{A}$ from the equations of motion and boundary conditions, and the subsequent construction of the scattering matrices, are given in Section 2 and Appendix A and B. Results of the MMPM are presented in Section 3. The method is first validated in 2D by comparison with FEM. In 3D, the accuracy of the method is tested on one configuration studied in Ref. [5], which serves to illustrate the convergence with respect to the radial and circumferential maximum mode orders used in the calculation. Finally, the ability of the method to treat realistic turbofan engine intakes configurations is checked.

## 2. Multi-modal propagation method

### 2.1. Derivation of the equations

A segmented lined duct with arbitrary impedance variations along the circumference is depicted in Fig. 1. Segments 0 and $L+1$ are supposed to be rigid and semi-infinite. Linear and lossless

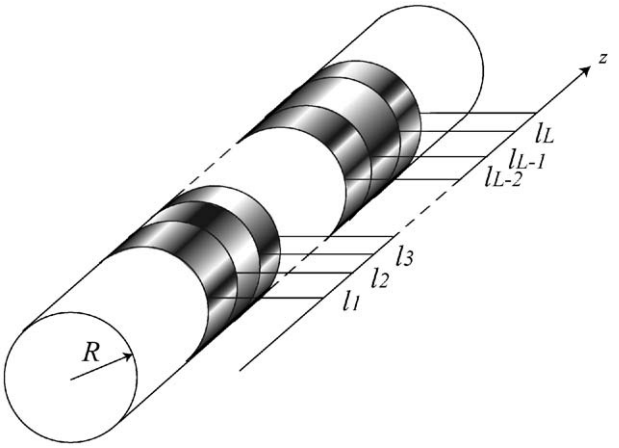


Fig. 1. Segmented lined duct with arbitrary impedance variations along the circumference.

sound propagation in air is assumed. With time dependence $\exp(j\omega t)$ omitted, the equation of mass conservation combined with the equation of state, and the equation of momentum conservation are written as

$$\nabla \cdot \mathbf{v} = -\frac{j\omega}{\rho_0 c_0^2} p, \tag{1}$$

$$j\omega \mathbf{v} = -\frac{1}{\rho_0} \nabla p, \tag{2}$$

where $\mathbf{v}$ is the particle velocity, $p$ the acoustic pressure, and $\rho_0$ and $c_0$ the ambient density and speed of sound in air. Pressures, velocities and lengths are, respectively, divided by $\rho_0 c_0^2$, $c_0$ and $R$ (the duct radius) to reduce Eqs. (1)–(2) to the dimensionless form

$$\nabla \cdot \mathbf{v} = -jKp, \tag{3}$$

$$-jK\mathbf{v} = \nabla p, \tag{4}$$

where $K = \omega R/c_0$ is the dimensionless wavenumber. This yields the 3D wave equation

$$\nabla_\perp^2 p + \frac{\partial^2 p}{\partial z^2} + K^2 p = 0, \tag{5}$$

where

$$\nabla_\perp^2 = \frac{1}{r}\frac{\partial}{\partial r}\left(r\frac{\partial}{\partial r}\right) + \frac{1}{r^2}\frac{\partial^2}{\partial \theta^2}. \tag{6}$$

The radial boundary condition is

$$\frac{\partial p}{\partial r} = Yp \quad \text{at } r = 1, \tag{7}$$

where $Y = -\mathrm{j}K\beta_0(z,\theta)$; here, $\beta_0(z,\theta)$ is the liner admittance. Following Pagneux et al. [6], the pressure $p$ and axial velocity $v_z$ are expressed using infinite series

$$p(r,\theta,z) = \sum_{m=-\infty}^{\infty} \sum_{n=0}^{\infty} P_{mn}(z)\Psi_{mn}(r,\theta), \tag{8}$$

$$v_z(r,\theta,z) = \sum_{m=-\infty}^{\infty} \sum_{n=0}^{\infty} V_{mn}(z)\Psi_{mn}(r,\theta), \tag{9}$$

where $P_{mn}$ and $V_{mn}$ are the modal coefficients. The projection functions $\Psi_{mn}$,

$$\Psi_{mn} = \frac{1}{\sqrt{\pi \Lambda_{mn}}} \mathrm{e}^{-\mathrm{j}m\theta} \frac{J_m(\alpha_{mn} r)}{J_m(\alpha_{mn})}, \tag{10}$$

are the eigenfunctions of the hard-walled cylindrical circular duct which obey the transverse Laplacian eigenproblem

$$\left[\frac{1}{r}\frac{\partial}{\partial r}\left(r\frac{\partial}{\partial r}\right) - \frac{1}{r^2}m^2\right]\Psi_{mn} = -\alpha_{mn}^2 \Psi_{mn}, \tag{11}$$

with hard-walled boundary condition

$$\frac{\partial \Psi_{mn}}{\partial r} = 0 \quad \text{at } r = 1, \tag{12}$$

and the orthogonality relation,

$$\int \Psi_{mn}(r,\theta)\Psi^*_{m'n'}(r,\theta)\,\mathrm{d}S = \delta_{m,m'}\delta_{n,n'}, \tag{13}$$

where the star denotes the complex conjugate. The normalization coefficients $\Lambda_{mn}$ are as follows:

$$\Lambda_{mn} = 1 - \frac{m^2}{\alpha_{mn}^2}. \tag{14}$$

The pressure and velocity fields $p$ and $v_z$ can always be projected over the eigenfunctions $\Psi_{mn}$ because the latter forms a complete basis of orthogonal functions. It can be noted that $\alpha_{mn}^2 = K^2 - K_{0z,mn}^2$, where $K_{0z,mn}$ are the normal mode axial wavenumbers of the hard-walled duct.

Following the matricial terminology, Eqs. (8) and (9) are written as

$$p(r,\theta,z) = \mathbf{\Psi}^{\mathrm{T}}\mathbf{P}, \tag{15}$$

$$v_z(r,\theta,z) = \mathbf{\Psi}^{\mathrm{T}}\mathbf{V}, \tag{16}$$

where $\mathbf{P}$, $\mathbf{V}$ and $\mathbf{\Psi}$ are column vectors. The superscript '$\mathrm{T}$' indicates the transpose. Rewriting Eqs. (3) and (4) with this terminology leads to

$$\mathbf{P}' = -\mathrm{j}K\mathbf{V}, \tag{17}$$

$$\mathbf{V}' = -\mathrm{j}K\left(\mathsf{I} - \frac{\mathsf{L}^2}{K^2}\right)\mathbf{P} - \frac{\mathrm{j}}{K}\,\mathsf{C}\,\mathbf{P}, \tag{18}$$

where the matrix $\mathsf{C}$ defined by

$$\mathsf{C}(z) = \int_0^{2\pi} \mathbf{\Psi}^*(1,\theta)\, Y(z,\theta) \mathbf{\Psi}^{\mathrm{T}}(1,\theta)\, \mathrm{d}\theta, \tag{19}$$

represents (hard-walled) mode coupling due to the liner. The prime indicates the derivative along the axial direction $z$ and $\mathsf{I}$ refers to the identity matrix. $\mathsf{L}$ is a diagonal matrix with $\alpha_{mn}$ on the diagonal. The detailed derivation of Eqs. (18)–(19) is given in Appendix A.

Now, considering that the admittance $Y(z,\theta)$ is piecewise constant along the $z$-axis, the two first-order Eqs. (17)–(18) may be combined to yield the following evolution equation:

$$\mathbf{P}'' + \mathsf{A}\mathbf{P} = \mathbf{0}, \tag{20}$$

with piecewise constant matrix $\mathsf{A}$ given by

$$\mathsf{A}(z) = (K^2\mathsf{I} - \mathsf{L}^2) + \mathsf{C}(z). \tag{21}$$

At the junctions $z = l_i$ between different segments, the continuity of the pressure and axial velocity requires continuity of vectors $\mathbf{P}$ and $\mathbf{P}'$ . In practice, the problem has to be truncated at a suitable truncation number $N_t$ which corresponds to the total number of components used to represent the field, and $\mathsf{A}$ is an $N_t \times N_t$ matrix.

### 2.2. *Coupling matrix* $\mathsf{C}$

From Eq. (21) the matrix $\mathsf{A}$ is the sum of two terms. The first diagonal term comes from using, as our fundamental set of basis functions, the fixed hard-walled duct basis. Hard-walled duct modes do not satisfy the wall boundary conditions, and thus the presence of the second coupling term $\mathsf{C}$, which may be viewed as the expression of intermodal scattering effects induced by the lining on the hard-walled duct modes. The elements of $\mathsf{C}$ are expressed as

$$\mathsf{C}_{mn,m'n'} = \frac{1}{\pi\sqrt{\Lambda_{mn}\Lambda_{m'n'}}} \int_0^{2\pi} Y(\theta) \mathrm{e}^{-\mathrm{j}(m'-m)\theta}\, \mathrm{d}\theta, \tag{22}$$

and, as such, are directly related to the coefficients of the Fourier series of $Y(\theta)$. In the case of uniform admittance, the only non-zero coupling terms are for modes of same circumferential order $m' = m$. In the case of non-uniform periodic admittance (with $N_Y$ periods within $2\pi$), additional coupling occurs between modes of different circumferential orders, such as $m - m' = \pm pN_Y$, where $p$ is an arbitrary integer. When the non-uniformities are caused by the presence of longitudinal splices, a general expectation on the amplitude distribution of such scattering may be obtained by considering the distribution of the Fourier coefficients $\frac{1}{2\pi}\int_0^{2\pi} Y(\theta)\mathrm{e}^{-\mathrm{j}m\theta}\,\mathrm{d}\theta$, where $Y(\theta)$ is considered to be equal to 1 at the lined parts and equal to zero on the splices. An illustration for three splices of same dimensions, resp., small, intermediate and large, is given in Fig. 2, where the above coefficients are reported as a function of $m$ (difference of circumferential mode orders in the scattering problem). Small splices are not efficient to scatter the incident mode over modes of different circumferential mode orders: scattering is concentrated on the incident circumferential mode order. Intermediate ones produce a broader distribution over the different circumferential mode orders. Large ones produce a large distribution of circumferential mode orders, however, of small amplitude.

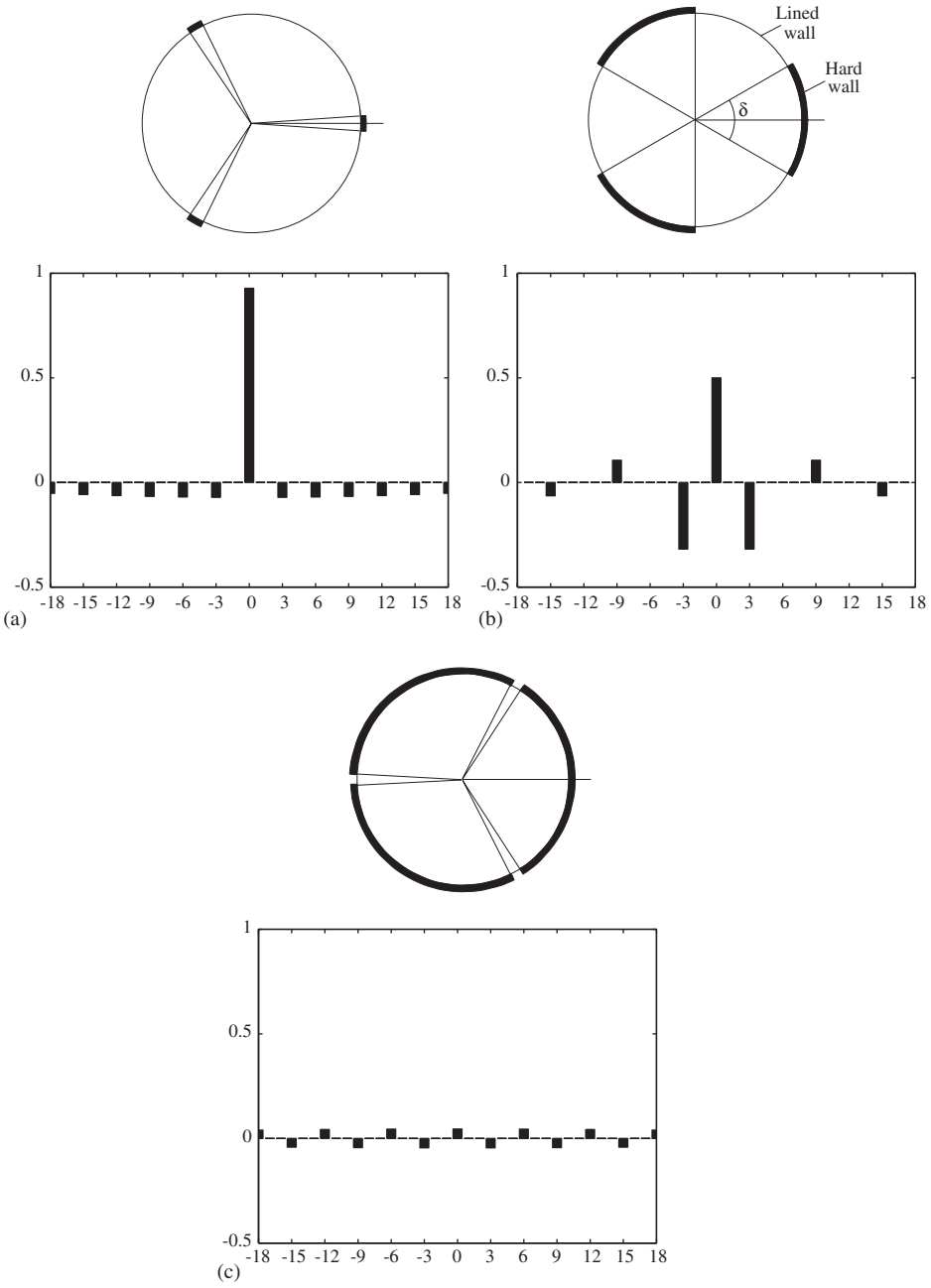


Fig. 2. Fourier series of the characteristic admittance function $Y$ for 3 different spliced configurations: (a) $\delta = 0.15$ rad, (b) $\delta = \pi/6$ rad and (c) $\delta = 1$ rad.

### 2.3. Scattering matrices

To construct the global scattering matrix of the segmented liner, we first express the scattering matrix for the simple configuration depicted in Fig. 3. It consists of one single-lined segment ($l_1 < z < l_2$) and two semi-infinite hard-walled ducts at both ends. The pressures of ingoing waves projected on the hard-walled eigenfunction basis, $\mathbf{A_1}$ and $\mathbf{B_2}$, are related to the pressures of outgoing waves, $\mathbf{A_2}$ and $\mathbf{B_1}$, by a scattering matrix $\mathsf{S}$

$$\begin{pmatrix} \mathbf{A_2} \\ \mathbf{B_1} \end{pmatrix} = \mathsf{S} \begin{pmatrix} \mathbf{A_1} \\ \mathbf{B_2} \end{pmatrix}, \quad \text{where } \mathsf{S} = \begin{bmatrix} \mathsf{T} & \mathsf{r} \\ \mathsf{R} & \mathsf{t} \end{bmatrix}. \tag{23}$$

$\mathbf{A_1}$, $\mathbf{B_1}$, $\mathbf{A_2}$ and $\mathbf{B_2}$ are continuous at those interfaces. This makes it very simple to construct the global scattering matrix. The reflection and transmission matrices are easily identified by writing the general field solution in the lined section and the continuity conditions at the interfaces. The general solution of Eq. (20) is

$$\mathbf{P} = \mathsf{X}\mathsf{D}(z)\mathbf{C_1} + \mathsf{X}\mathsf{D}^{-1}(z)\mathbf{C_2}, \tag{24}$$

where $\mathbf{C_1}$ and $\mathbf{C_2}$ are amplitude vectors of dimension $N_t$, $\mathsf{X}$ is the $N_t \times N_t$ matrix whose columns are the eigenvectors $\mathbf{X}_n$ of matrix $\mathsf{A}$, and $\mathsf{D}(z)$ and $\mathsf{D}^{-1}(z)$ are diagonal matrices with $\exp(-\mathrm{j}v_n z)$ and $\exp(\mathrm{j}v_n z)$, respectively, on the main diagonal, with $v_n = \sqrt{d_n}$, $d_n$ being the eigenvalues of matrix $\mathsf{A}$. Before proceeding, it is convenient to rewrite Eq. (24), by redefining the amplitude coefficients $\mathbf{C_1}$ and $\mathbf{C_2}$ as

$$\mathbf{P} = \mathsf{X}\mathsf{D}(z - l_1)\mathbf{C_1} + \mathsf{X}\mathsf{D}(l_2 - z)\mathbf{C_2}. \tag{25}$$

In the form of Eq. (25), numerical stability is ensured because the propagation matrices $\mathsf{D}(z - l_1)$ and $\mathsf{D}(l_2 - z)$ have only positive arguments and contain no exponentially diverging terms due to the evanescent modes.

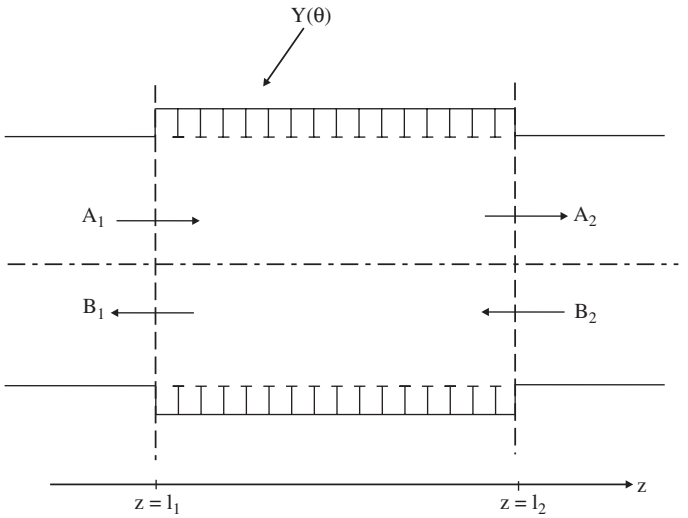


Fig. 3. Single element, input/output amplitudes.

The continuity of pressure and axial velocity leads to

$$\mathbf{A_1} + \mathbf{B_1} = \mathsf{X}(\mathbf{C_1} + \mathsf{D}_{1,2}\mathbf{C_2}),$$

$$\mathsf{K}_0(\mathbf{A_1} - \mathbf{B_1}) = \mathsf{X}\mathsf{K}_\mathsf{Y}(\mathbf{C_1} - \mathsf{D}_{1,2}\mathbf{C_2}),$$

$$\mathbf{A_2} + \mathbf{B_2} = \mathsf{X}(\mathsf{D}_{1,2}\mathbf{C_1} + \mathbf{C_2}),$$

$$\mathsf{K}_0(\mathbf{A_2} - \mathbf{B_2}) = \mathsf{X}\mathsf{K}_\mathsf{Y}(\mathsf{D}_{1,2}\mathbf{C_1} - \mathbf{C_2}), \tag{26}$$

where $\mathsf{D}_{1,2} = \mathsf{D}(l_2 - l_1)$, and $\mathsf{K}_0$ and $\mathsf{K}_\mathsf{Y}$ are the diagonal matrices with the axial wavenumbers on diagonal in the rigid and lined sections (resp., the $K_{0z,mn}$ and $d_n$). By denoting

$$\mathsf{F} = \mathsf{X} + \mathsf{K}_0^{-1}\mathsf{X}\mathsf{K}_\mathsf{Y},$$

$$\mathsf{G} = \mathsf{X} - \mathsf{K}_0^{-1}\mathsf{X}\mathsf{K}_\mathsf{Y},$$

Eq. (26) is reduced to

$$2\mathbf{A_1} = \mathsf{F}\mathbf{C_1} + \mathsf{G}\mathsf{D}_{1,2}\mathbf{C_2},$$

$$2\mathbf{B_1} = \mathsf{G}\mathbf{C_1} + \mathsf{F}\mathsf{D}_{1,2}\mathbf{C_2},$$

$$2\mathbf{A_2} = \mathsf{F}\mathsf{D}_{1,2}\mathbf{C_1} + \mathsf{G}\mathbf{C_2},$$

$$2\mathbf{B_2} = \mathsf{G}\mathsf{D}_{1,2}\mathbf{C_1} + \mathsf{F}\mathbf{C_2}. \tag{27}$$

The reflection and transmission matrices, which completely characterize the segmented liner, are then given by

$$\mathsf{T} = \mathsf{t} = (\mathsf{F}\mathsf{D}_{1,2} - \mathsf{G}\mathsf{F}^{-1}\mathsf{G}\mathsf{D}_{1,2})(\mathsf{F} - \mathsf{G}\mathsf{D}_{1,2}\mathsf{F}^{-1}\mathsf{G}\mathsf{D}_{1,2})^{-1},$$

$$\mathsf{R} = \mathsf{r} = (\mathsf{G} - \mathsf{F}\mathsf{D}_{1,2}\mathsf{F}^{-1}\mathsf{G}\mathsf{D}_{1,2})(\mathsf{F} - \mathsf{G}\mathsf{D}_{1,2}\mathsf{F}^{-1}\mathsf{G}\mathsf{D}_{1,2})^{-1}. \tag{28}$$

Then, knowing the scattering matrices of two different elements, the scattering matrix of the compound element made by the juxtaposition of the two may be directly written by using a simple composition law $\otimes$, which is recalled in Appendix B. The global scattering matrix of the segmented liner is then obtained by composing the scattering matrix of each segment $\mathsf{S}_\mathsf{i}$ defined by Eq. (23) as follows:

$$\mathsf{S}_{\mathsf{tot}} = \mathsf{S}_{\mathsf{I}_1} \otimes \mathsf{S}_{\mathsf{I}_2} \otimes \cdots \otimes \mathsf{S}_{\mathsf{I}_\mathsf{L}}. \tag{29}$$

## 3. Results

### 3.1. Validation and convergence of the Multi-Modal Propagation Method

To validate the MMPM, we compare the results with those of FEM in Partial Differential Equation (PDE) Toolbox of Matlab. The PDE Toolbox defines a 2D PDE problem with local boundary conditions and provides the solution using an FEM technique. We consider an infinite rigid rectangular duct with a uniform liner in the side $y' = 0$ along the $x'$ direction. A typical

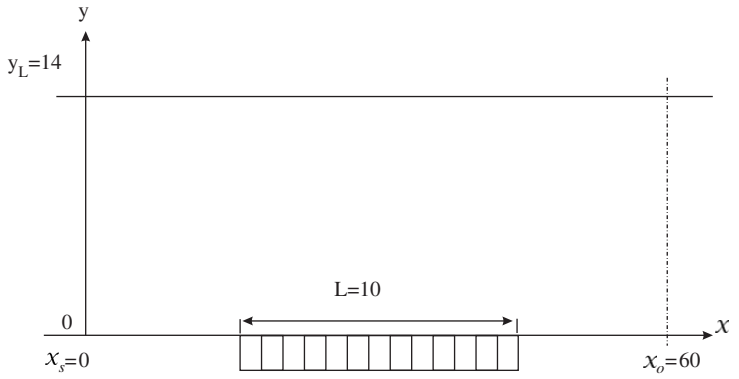


Fig. 4. Configuration of validation.

dimensionless lining admittance $\beta_0 = 1 + \mathrm{j}$ is chosen. For convenience to compare with the results of FEM here, we use dimensionless length variables, $x = kx'$ and $y = ky'$, where $k = \omega/c$. The source plane is at $x_s = 0$ and the output plane is at $x_o = 60$. The dimensionless length of the liner is $L = 10$. The liner is at $25 \leqslant x \leqslant 35$. The dimensionless height of the duct $y_L = ky'_L$, which will be taken at three different values (3, 14, 50), has the direct meaning of the dimensionless wavenumber $K$ ($K = 3, 14, 50$). The configuration is shown in Fig. 4 for the special choice $y_L = K = 14$. The boundary conditions at the lining wall $y = 0$, $25 \leqslant x \leqslant 35$, for the FEM and the MMPM are

$$\frac{\partial p}{\partial y} = -\mathrm{j}(1 + \mathrm{j})p. \tag{30}$$

The boundary conditions at the rigid wall ($y = 0$, $0 \leqslant x < 25$, $35 < x \leqslant 60$ and $y = K$, $0 \leqslant x \leqslant 60$) for both the FEM and MMPM are

$$\frac{\partial p}{\partial y} = 0. \tag{31}$$

At the radiation plane $x = x_o$ and the source plane $x = x_s$, we have to set local boundary conditions,

$$\frac{\partial p}{\partial x} + gp = q, \tag{32}$$

(where $g$ and $q$ are arbitrary functions of $y$) in order that the problem can be solved in PDE Toolbox of Matlab.

For the sake of simplicity, we chose the boundary condition at $x = x_o$ as

$$\frac{\partial p}{\partial x} + \mathrm{j}p = 0, \tag{33}$$

In MMPM language this is equivalent to imposing the condition $\mathbf{V} = \mathbf{P}$ at $x = x_o$. We refer to this boundary condition as 'artificial boundary condition' in contrast to the exact radiation condition.

Similarly, we chose the following boundary condition at $x = x_s$

$$\frac{\partial p}{\partial x} - \mathrm{j}p = -2\mathrm{j}\Psi_n. \tag{34}$$

where $\Psi_n = \cos(n\pi y/y_L)$ is the eigenfunction of the incident rigid mode $n$.

In MMPM language this is equivalent to imposing the 'artificial boundary condition' $\mathbf{V} = 2\mathbf{I}_1 - \mathbf{P}$ at $x = x_s$, where $\mathbf{I}_1$ refers to $(\delta_{1,n}, \delta_{2,n}, \delta_{3,n} \cdots)^{\mathrm{T}}$, 'T' refers to transpose, $\delta$ refers to Kronecker delta and $n$ is the order of the incident mode as above.

In what follows, results of sound pressure contours and profiles obtained by FEM will be compared to those obtained with MMPM using the above 'artificial boundary conditions'.

One first test (not shown in figures) is done for a dimensionless transverse width $K = 3$. At such low frequency, only the mode $(0, 0)$ propagates. The MMPM solution is in excellent agreement with the FEM solution.

Two examples of increasing the frequency of calculation are presented. One is for dimensionless wavenumber $K = 14$, 5 propagating modes are cut-on, the first mode ($n = 0$) is incident. 30 rigid modes are used to assure the MMPM convergence. The other is for dimensionless wavenumber $K = 50$, 16 propagating modes are cut-on, the third mode ($n = 2$) is incident. Sixty rigid modes are used to assure the MMPM convergence. $K = 50$ is approximately the maximum wavenumber that can be calculated on a PC with PDE toolbox.

The contours of the pressure modulus computed by FEM and MMPM are firstly compared. The patterns agree very well to show the MMPM achieving a correct result. Figs. 5 and 6 show them for $K = 14$.

Next, we plot on Fig. 7 the sound pressure profiles on one given section, $x = 29.86$ for $K = 14$ and 50. This section is in the lined part of the duct. At $y/y_L = 0$, the sound pressure satisfies the

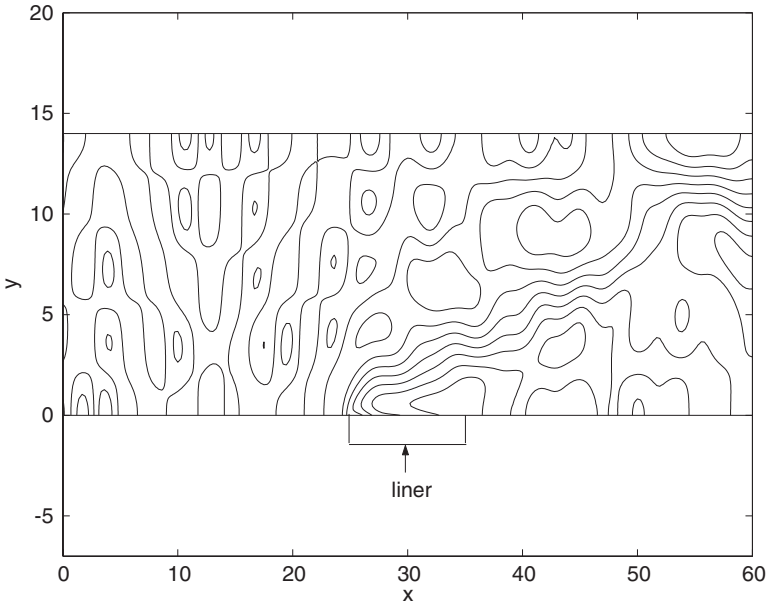


Fig. 5. Sound pressure contour by the FEM.

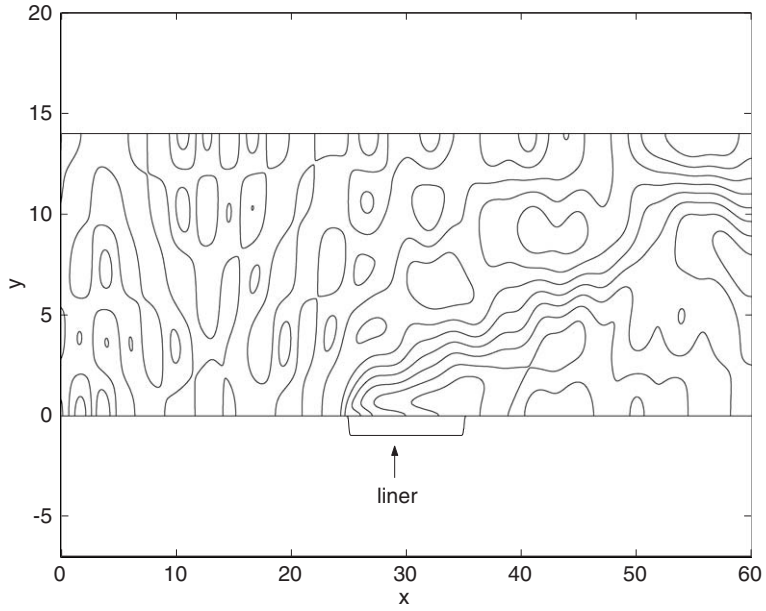


Fig. 6. Sound pressure contour by MMPM with 'artificial boundary condition'.

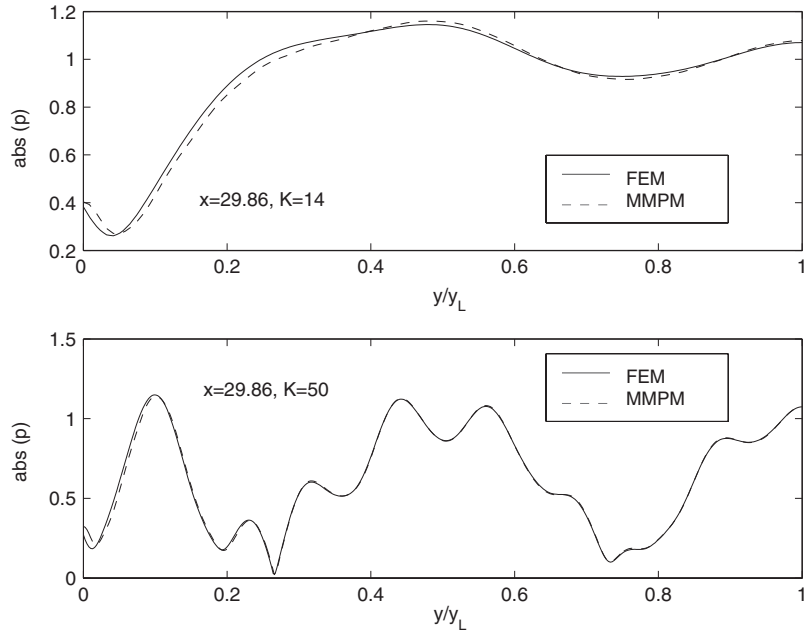


Fig. 7. The transverse profile of sound pressure modulus at $x = 29.86$, for $K = 14$ (top) and $K = 50$ (bottom); at $y/y_L = 0$, the sound pressure satisfies the lining impedance boundary condition, and at $y/y_L = 1$, the boundary condition is rigid. '–', FEM; '––', MMPM with 'artificial boundary conditions'.

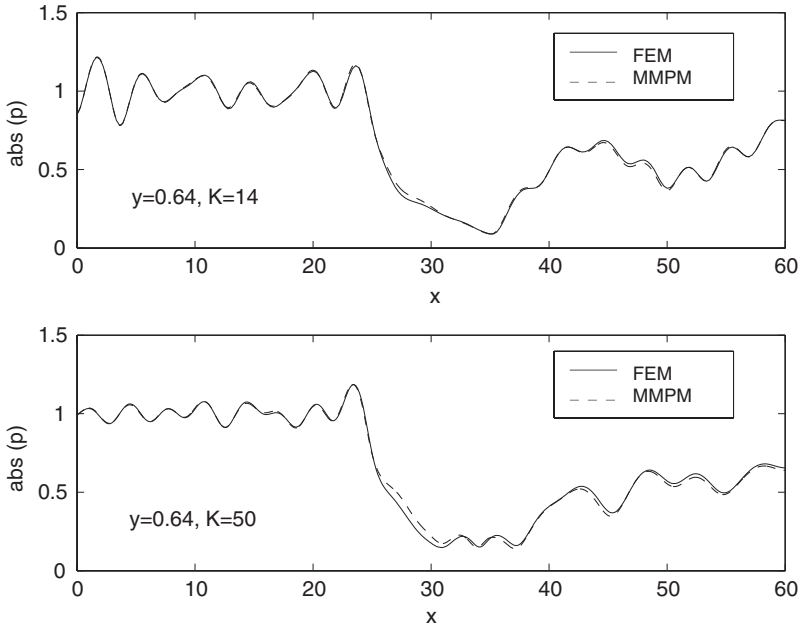


Fig. 8. The axial profiles of sound pressure modulus at $y = 0.64$, near liner, for $K = 14$ (top) and $K = 50$ (bottom); '–', FEM; '––', MMPM with 'artificial boundary conditions'.

lining impedance boundary condition, and at $y/y_L = 1$, the boundary condition is rigid. The two calculations are close, showing that the MMPM is working. When we zoom in near the liner, there appears a small layer in which the pressure slope quickly goes to zero. This is an effect due to truncating the series at a finite number of components.

The axial profiles of sound pressure modulus and phases are shown in Figs. 8 and 9 for $K = 14$ and 50, respectively. The values of sound pressure are chosen at $y = 0.64$, which is relatively close to the liner. The MMPM shows good agreement with the FEM solution.

For the 3D case, we compare the results of the MMPM with those of FEM given in Ref. [5]. As discussed above, a spliced liner with intermediate size of splices will efficiently scatter one incident mode on modes of different circumferential orders. Configuration 4 in Ref. [5], which is sketched in the present Fig. 10, is one example of a such spliced liner. This configuration is defined by a lined section of length $L = 2a$, where $a$ is the duct radius, two splices of angle $\psi = 0.75$ rad, a dimensionless wavenumber equal to $K = 6.8$ and an admittance parameter given by $Y = 2.247 - 2.566\mathrm{j}$. Output modal amplitudes of the propagative modes for input mode $(m, n) = (1, 0)$ are given in Fig. 11 (resp., [5], Fig. 12). In this calculation the circumferential maximum modal order $m$ is taken equal to 16, and 20 radial modes are taken into account. (This includes all propagative and some of the evanescent modes.) The results have the same global shape as those in Ref. [5]; however, some discrepancies in the values occur.

Indications on the convergence of the MMPM results are given in Fig. 12, where $M$ and $N$ are circumferential and radial truncation mode orders, respectively. Let us denote by $p$ the variable output pressure field calculated when using variable values of $M$ and $N$, and by $p_{\mathrm{ref}}$ the output pressure field calculated when using reference maximum values of the truncation numbers

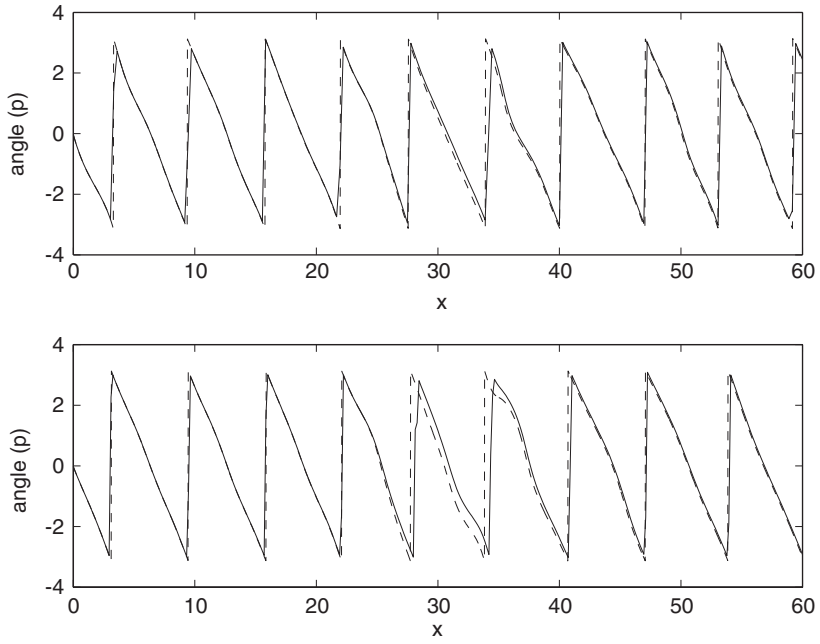


Fig. 9. The axial profiles of sound pressure phase at $y = 0.64$, near liner, for $K = 14$ (top) and $K = 50$ (bottom); '−', FEM; '−−', MMPM with 'artificial boundary conditions'.

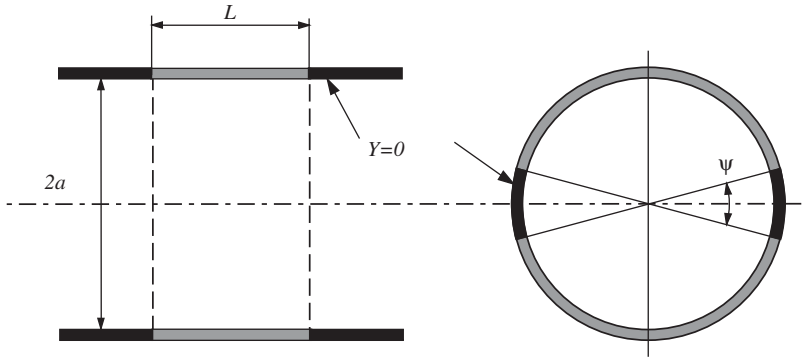


Fig. 10. Test configuration with 2 splices. $\psi = 0.75\,\text{rad}$ , $L/a = 2$, $K = 6.8$ and $Y = 2.247 - 2.566\text{j}$.

$(M_{\text{ref}}, N_{\text{ref}})$. Then, we define an error indicator $\varepsilon$ as

$$\varepsilon = \sqrt{\frac{\int_s \|p - p_{\text{ref}}\|^2 \, \mathrm{d}S}{\int_s \|p_{\text{ref}}\|^2 \, \mathrm{d}S}}. \tag{35}$$

To study the convergence of the method with respect to the circumferential modal order, we set $(M_{\text{ref}}, N_{\text{ref}}) = (75, 20)$ and plot in Fig. 12 the values of $\log_{10} \varepsilon(M, 20)$ with $M$ varying in the range

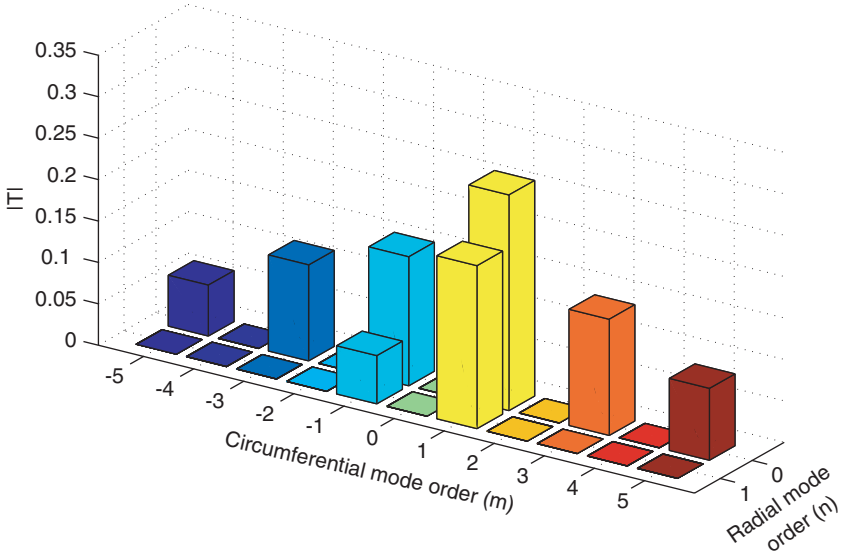


Fig. 11. Modulus of transmitted sound pressure modal amplitudes for incident mode $(m, n) = (1, 0)$.

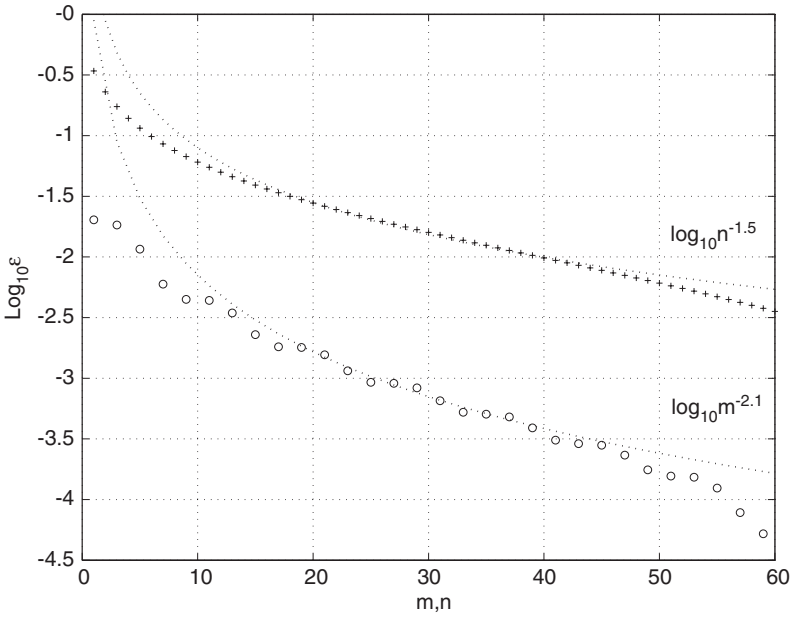


Fig. 12. MMPM errors $\log_{10}\varepsilon$ versus truncation numbers $M$ and $N$. '$\circ$' denotes $N = 20$ fixed, $M$ variable $(1 - 60)$, '$+$' denotes $M = 16$ fixed, $N$ variable $(1 - 60)$.

1–60. To study the convergence of the method with respect to the radial modal order, we set $(M_{\text{ref}}, N_{\text{ref}}) = (16, 80)$ and plot in Fig. 12 the values of $\log_{10}\varepsilon(16, N)$ with $N$ varying in the range 1–60. The decay rate of the error indicator $\varepsilon$ versus $M$ or $N$ is estimated in an intermediate range

of values of numbers $M$ or $N$. The values of either $M$ or $N$ are sufficiently large to yield a pertinent estimate of this decay rate, and sufficiently small to avoid the bias due to the finite values of the reference values $M_{\text{ref}}$ or $N_{\text{ref}}$. The first type of variations, indicated with symbol 'o', show that the decay rate of the error is at least $O(M^{-2})$. The second type of variations, indicated with symbol '+', illustrates a slower decay rate of the error versus $N$. The latter is found to be $O(N^{-1.5})$. These decay rates are obtained for large enough $M$ or $N$, meaning that the error passes the initial transition parts and has a uniform comportment. Values of $M$ and $N$ for the transition obviously depend on the particulars of the configuration (such as, frequency, nature of the incident field and liner impedance).

In general, we may say that this method has good convergence properties in circumferential direction. When the impedance variations versus $\theta$ are smooth, say $Z(\theta) = \sin\theta$, this method will converge more rapidly. Convergence properties in radial direction are weaker, because the expansion basis functions do not meet the wanted impedance boundary conditions. To be represented by the superposition of hard-walled duct basis functions, the latter boundary conditions require considering a large number of components of different radial numbers. Nevertheless, in the example studied, we expect on the basis of Fig. 12 that our results of Fig. 11 have a relative precision on the order of 3%, which seem to indicate that the discrepancies between our results and those of Ref. [5] are not to be attributed to the MMPM truncation errors.

### 3.2. *Effect of circumferential non-uniform lining*

In this section, we illustrate the ability of the MMPM to treat realistic turbofan engine intakes configurations.

The first example is to show the effects of hard-walled longitudinal splices. The sound power transmission loss of the liner ($-10\log_{10} W_o/W_i$), with or without hard-walled splices, is plotted for two different, well-attenuated modes in Fig. 13. The parameters of the configuration are from Ref. [5]. We consider a one segment liner with two hard-walled splices diametrically opposed and given by an angle of 0.15 rad. The reduced wavenumber and impedance are $K = 20$ and $Z/\rho c = 2 - \mathrm{j}$, respectively. Modes (17, 0) and (13,0) are incident. The mode (17, 0) is the last propagating mode in the hard-walled duct. In general, in the turbofan engine, the lining admittance and the splices angles are not large. Thus, the modes coupling effects introduced by the presence of splices are small, because the components $m = 1, 2\ldots$ of the Fourier transformation of $Y(\theta)$ are small compared to the term $m = 0$. In general, it is expected that these couplings will have a small effect on the attenuation of the liner. Fig. 13 presents precisely one exception to this, due to the highly attenuated nature of the field. When the incident mode is highly attenuated, which is especially the case of the (near cut-off) mode (17, 0), the small scattering due to the presence of splices will produce lower order components, much less attenuated, that are important to consider if one wishes to predict correctly the value of the transmitted power through the lined segment. In this case, even if the additional scattering due to the splices is small, the resulting output power may be much higher for the spliced configuration than for the uniform configuration. This effect remains noticeable for the mode (13,0), which is also relatively highly attenuated in the uniform configuration.

To assess the calculating capability of our method, two examples are presented. The first one is mode scattering induced by turbofan spliced intake liner at BPF. For this example, the following

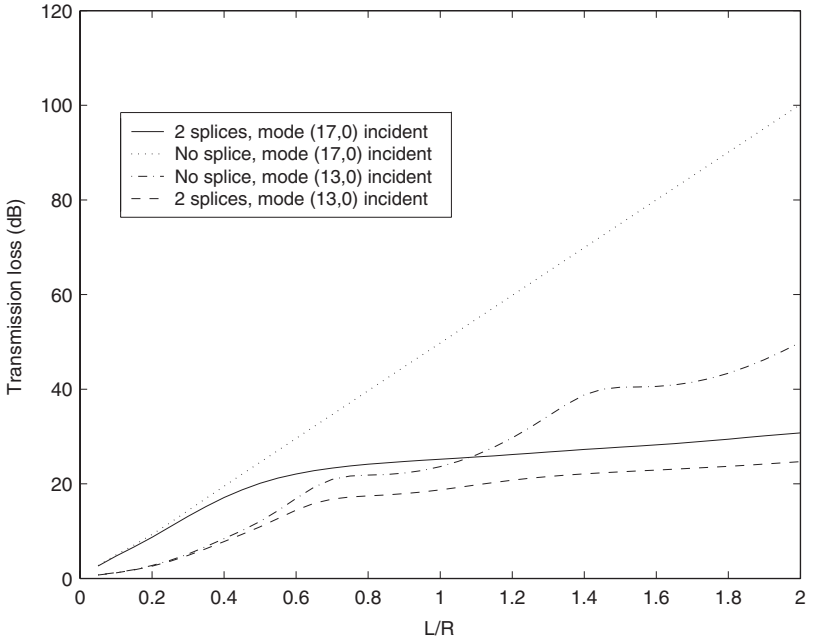


Fig. 13. The penalty effects of longitudinal splices at high frequencies, for highly attenuated modes are transmission loss versus the dimensionless lining length $L/R$. The configuration parameters are $K = 20$, $Z/\rho c = 2 - \mathrm{j}$ and $\psi = 0.15$ rad. '–', 2 splices, input mode $(17, 0)$; '..', no splice, input mode $(17, 0)$; '––', 2 splices, input mode $(13, 0)$; '–.', no splice, input mode $(13, 0)$.

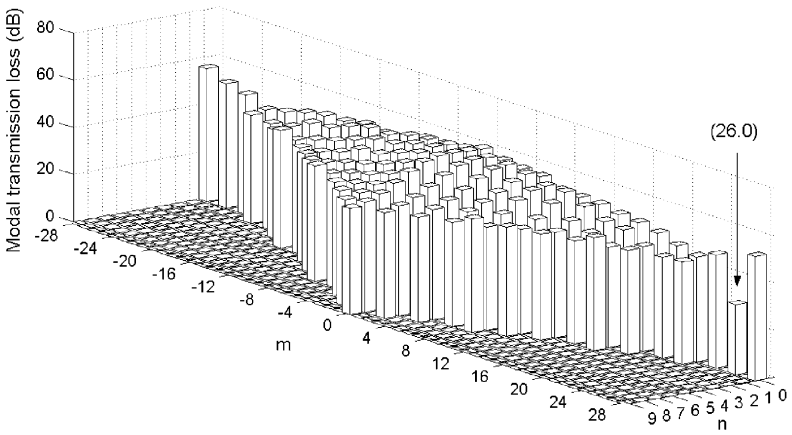


Fig. 14. Mode scattering induced by turbofan spliced intake liner at BPF. The parameters are incident 'rotor-alone' mode $m = 26$, $K = 31.26$, 2 splices with angles $\pi/60$, lining impedance $Z/\rho c = 2 - \mathrm{j}$ and lining length $L/R = 0.48$.

is assumed: incident 'rotor-alone' mode $m = 26$, dimensionless wavenumber $K = 31.26$, 2 hard-walled diametrically opposed splices with angles $\pi/60$, lining impedance $Z/\rho c = 2 - \mathrm{j}$, lining length $L/R = 0.48$. Mode scattering is shown in Fig. 14. Only even $m$-modes are coupled to the two hard-walled splices. Although modes $(\pm 28, 0)$ are coupled, a large number of lower-order

modes is excited and the performance of the liner decreases. After calculating the total in-duct transmitted energy flux, it is shown that there is about 6 dB less attenuation with splices than without splices.

The configuration of a more difficult example is as shown in Fig. 15. The lining includes two axial segments with the same length $L = 0.275/R$, $R = 0.865$ m. The first segment is uniform with impedance $Z_0/\rho c = 0.5 - 0.2$j, the second segment includes four equal-sized, uniform circumferential segments with impedance $Z_i/\rho c$ $(i = 1 - 4)$ given by $1.2 - 1.7$j, $1.2 - 3$j, $1.2 - 1.5$j and $1.2 - 0.2$j, respectively. The reduced frequency is $K = 46.5$; 565 modes propagate. Mode $(26, 0)$ is incident. In this configuration, we have both a very high reduced wavenumber and a non-uniform lining. This example may be very difficult to treat with other methods such as FEM. To the knowledge of the authors, no results for 3D liners at such high frequencies have been published. The modal transmission loss at the exit plane (defined as $-10\log_{10} W_{mn}/W_i$) is shown in Fig. 16. This figure shows that the predominant modes (the modes which have the least transmission loss)

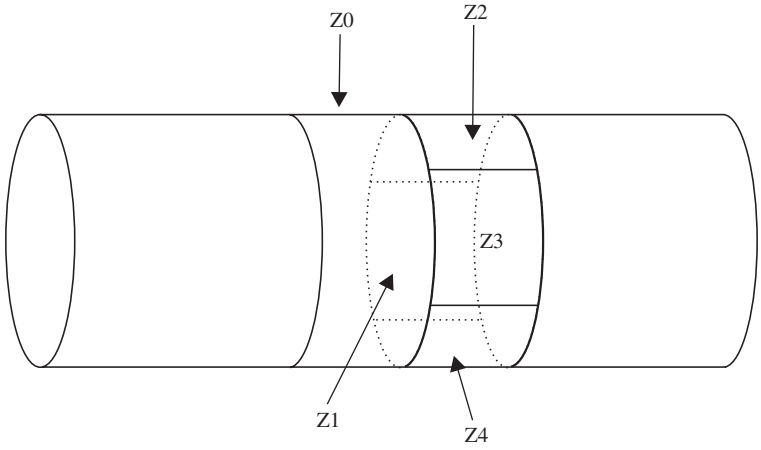


Fig. 15. Configuration of two segment liner.

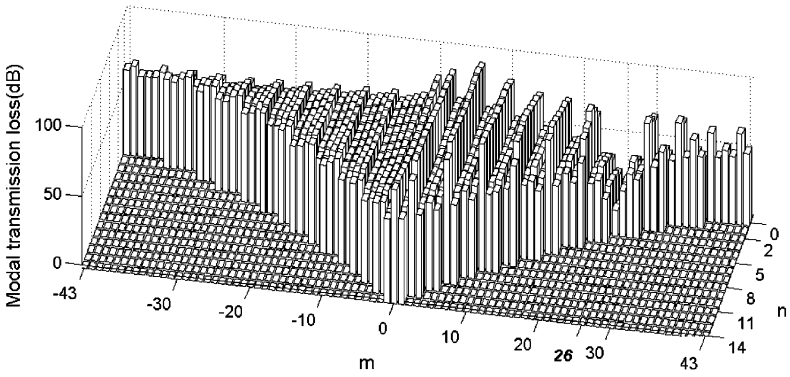


Fig. 16. Modal transmission loss of the above configuration.

at the exit plane are essentially modes $m = 26$ and $n = 0, 1, 2, 3$. Modes $m = 23, 24, 25, 27, 28, 29$, whose $m$-orders of modes are close to $m = 26$, are excited a little stronger than the others. It is shown that for this configuration without rigid splices, although the impedance at the second segment is circumferential non-uniform, the circumferential modes coupling is not strong.

## 4. Conclusion

An MMPM is validated to study sound propagation in a hard-walled circular cylindrical duct lined with non-uniform impedance in the absence of flow. The liner is piecewise constant along the duct and may arbitrarily vary along the circumference. The multimodal equations governing the components of the pressure and velocity projected on the hard-walled duct modes then show that their components obey a constant coefficient second-order differential matrix equation $\mathbf{P}'' + \mathsf{A}\mathbf{P} = 0$ in each segment. The sound field, taking into account the coupling between hard-walled duct modes, is easily expressed in terms of the eigenvalues and eigenfunctions of matrix $\mathsf{A}$ after truncation at a sufficient number of components. Mode-scattering effects because of the peripherally non-uniform impedance are clearly expressed in the Fourier transform of liner admittance $Y$. It is numerically shown that the convergence rate of the infinite series is at least $O(M^{-2})$ and $O(N^{-1.5})$, where $M$ and $N$ refer to the maximum circumferential and radial mode orders, respectively.

Simple matrix calculations yield the scattering matrix of one liner segment. The global scattering matrix is then easily obtained by the method of Furnell and Bies [13]. The great advantage of this method, in contrast to the FEM code, is that no discretization in the longitudinal direction is necessary. Much less memory is then required. Consequently, this method enables us to compute properties at quite high frequencies ($K \sim 50$).

Numerical calculations indicate that peripherally non-uniform liners have negligible modes scattering effects for typical configurations in turbofan engine, provided the overall power output considered is not governed by special, well-attenuated modes. For such modes, the presence of hard-walled splices may have a great penalty effect.

## Acknowledgements

The authors gratefully acknowledge support provided by a grant from SNECMA MOTEURS, France.

## Appendix A. Derivation of Eqs. (18)–(19)

Eq. (3) is rewritten as

$$\frac{\partial v_z}{\partial z} = -\mathrm{j}Kp - \boldsymbol{\nabla}_\perp \cdot \mathbf{v}_\perp = -\mathrm{j}Kp + \frac{1}{\mathrm{j}K}\nabla_\perp^2 p. \tag{A.1}$$

The term $\nabla_{\perp}^2 p$ is projected on the basis $\mathbf{\Psi}^*$ using Eqs. (7), (11) and (12),

$$\begin{aligned}\int \nabla_{\perp}^2 p \Psi_{mn}^* \,\mathrm{d}S &= \int p \nabla_{\perp}^2 \Psi_{mn}^* \,\mathrm{d}S + \oint \left( \Psi_{mn}^* \frac{\partial p}{\partial r} - p \frac{\partial \Psi_{mn}^*}{\partial r} \right) \mathrm{d}C \\ &= \int p(-\alpha_{mn}^2) \Psi_{mn}^* \,\mathrm{d}S + \oint \Psi_{mn}^*(1,\theta) Y p \,\mathrm{d}C \\ &= -\alpha_{mn}^2 P_{mn} + \int_0^{2\pi} \Psi_{mn}^*(1,\theta) Y \mathbf{\Psi}^{\mathrm{T}}(1,\theta) \mathbf{P} \,\mathrm{d}\theta. \end{aligned} \tag{A.2}$$

Using Eq. (A.2), the projection of Eq. (A.1) leads to Eqs. (18)–(19).

## Appendix B. Composition of the scattering matrices

The scattering matrices of two adjacent segments (see Fig. 17) are defined by

$$\begin{pmatrix} \mathbf{A_2} \\ \mathbf{B_1} \end{pmatrix} = \mathsf{S}_1 \begin{pmatrix} \mathbf{A_1} \\ \mathbf{B_2} \end{pmatrix}, \quad \text{where } \mathsf{S}_1 = \begin{bmatrix} \mathsf{T}_1 & \mathsf{r}_1 \\ \mathsf{R}_1 & \mathsf{t}_1 \end{bmatrix} \tag{B.1}$$

and

$$\begin{pmatrix} \mathbf{A}_3 \\ \mathbf{B_2} \end{pmatrix} = \mathsf{S}_2 \begin{pmatrix} \mathbf{A_2} \\ \mathbf{B}_3 \end{pmatrix}, \quad \text{where } \mathsf{S}_2 = \begin{bmatrix} \mathsf{T}_2 & \mathsf{r}_2 \\ \mathsf{R}_2 & \mathsf{t}_2 \end{bmatrix}. \tag{B.2}$$

Following Furnell and Bies [13], the scattering matrix of the two segments is given by

$$\begin{pmatrix} \mathbf{A}_3 \\ \mathbf{B_1} \end{pmatrix} = \mathsf{S}_{12} \begin{pmatrix} \mathbf{A_1} \\ \mathbf{B}_3 \end{pmatrix}, \quad \text{where } \mathsf{S}_{12} = \mathsf{S}_1 \otimes \mathsf{S}_2 = \begin{bmatrix} \mathsf{T}_{12} & \mathsf{r}_{12} \\ \mathsf{R}_{12} & \mathsf{t}_{12} \end{bmatrix}. \tag{B.3}$$

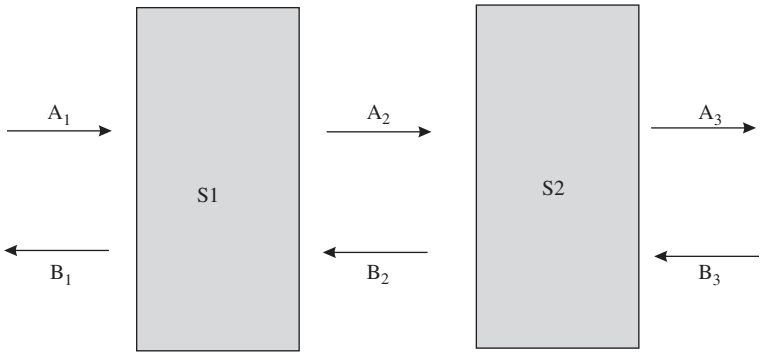


Fig. 17. Diagrammatic representation of two segments of lined duct.

The elements of the matrix $\mathsf{S}_{12}$ are given by

$$\mathsf{T}_{12} = \mathsf{T}_2\mathsf{E}\mathsf{T}_1, \quad \mathsf{t}_{12} = \mathsf{t}_1\mathsf{F}\mathsf{t}_2,$$

$$\mathsf{R}_{12} = \mathsf{R}_1 + \mathsf{t}_1\mathsf{F}\mathsf{R}_2\mathsf{T}_1, \quad \mathsf{r}_{12} = \mathsf{r}_2 + \mathsf{T}_2\mathsf{E}\mathsf{r}_1\mathsf{t}_2,$$

$$\mathsf{E} = (\mathsf{I} - \mathsf{r}_1\mathsf{R}_2)^{-1}, \quad \mathsf{F} = (\mathsf{I} - \mathsf{R}_2\mathsf{r}_1)^{-1}, \tag{B.4}$$

$\mathsf{I}$ being the identity matrix.

## References


[1] S.L. Sarin, E.R. Rademaker, In flight acoustic mode measurements in the turbofan engine inlet of Fokker 100 aircraft, AIAA paper 93-4414, 1993.

[2] W.R. Watson, Circumferentially segmented duct liners optimized for axisymmetric and standing-wave sources, NASA-2075, 1982.

[3] C.R. Fuller, Propagation and radiation of sound from flanged circular ducts with circumferentially varying wall admittances, I: semi-infinite ducts, *Journal of Sound and Vibration* 93 (1984) 321–340.

[4] C.R. Fuller, Propagation and radiation of sound from flanged circular ducts with circumferentially varying wall admittances, II: finite ducts with sources, *Journal of Sound and Vibration* 93 (1984) 341–351.

[5] B. Regan, J. Eaton, Modeling the influence of acoustic liner non-uniformities on duct modes, *Journal of Sound and Vibration* 219 (1999) 859–879.

[6] V. Pagneux, N. Amir, J. Kergomard, A study of wave propagation in varying cross-section waveguides by modal decomposition, part I: theory and validation, *Journal of the Acoustical Society of America* 100 (1996) 2034–2048.

[7] S. Felix, V. Pagneux, Sound propagation in rigid bends: A multimodal approach, *Journal of the Acoustical Society of America* 110 (2001) 1329–1337.

[8] S. Felix, V. Pagneux, Multi-modal analysis of acoustic propagation in three-dimensional bends, *Wave Motion* 36 (2002) 157–168.

[9] Recently, during preparation of this revised manuscript, the MMPM was applied to study the joint effects of liners and curvature: S. Felix, V. Pagneux, Sound attenuation in lined bends, *Journal of the Acoustical Society of America* 116 (2004) 1921–1931.

[10] V. Pagneux, A. Maurel, Lamb wave propagation in inhomogeneous elastic waveguide, *Proceedings of the Royal Society of London A* 458 (2002) 1913–1930.

[11] Y. Aurégan, M. Leroux, V. Pagneux, Measurement of liner impedance with flow by an inverse method, AIAA 2004-2838, 10th AIAA/CEAS Aeroacoustics Conference, Manchester, May 2004.

[12] A.H. Nayfeh, J.E. Kaiser, D.P. Telionis, Acoustics of aircraft engine-duct systems, *AIAA Journal* 13 (1975) 130–153.

[13] G.D. Furnell, D.A. Bies, Matrix analysis of acoustic wave propagation within curved ducting system, *Journal of Sound and Vibration* 132 (1989) 245–263.